

JGR Space Physics

RESEARCH ARTICLE

10.1029/2023JA031711

Key Points:

- A 1-D general curvilinear particle-in-cell simulation model is used to study the generation mechanisms of hiss-like emissions
- Based on the spectrogram, the hiss-like emissions are classified into four types (I, II, III, IV)
- The majority of hiss-like chorus waves in the Earth's magnetosphere are generated through a nonlinear process

Correspondence to:

X. Gao and Q. Lu,
gaoxl@mail.ustc.edu.cn;
qmlu@ustc.edu.cn

Citation:

Kong, Z., Gao, X., Lu, Q., & Wang, X. (2023). Generation mechanisms of hiss-like chorus in the Earth's magnetosphere. *Journal of Geophysical Research: Space Physics*, 128, e2023JA031711. <https://doi.org/10.1029/2023JA031711>

Received 19 MAY 2023

Accepted 10 OCT 2023

Author Contributions:

Conceptualization: Zhenyu Kong, Xinliang Gao, Quanming Lu
Investigation: Zhenyu Kong
Methodology: Zhenyu Kong
Project Administration: Xinliang Gao
Software: Zhenyu Kong, Xueyi Wang
Validation: Zhenyu Kong
Visualization: Quanming Lu
Writing – original draft: Zhenyu Kong
Writing – review & editing: Xinliang Gao

Generation Mechanisms of Hiss-Like Chorus in the Earth's Magnetosphere

Zhenyu Kong^{1,2,3,4} , Xinliang Gao^{1,2,3,4} , Quanming Lu^{1,2,3,4} , and Xueyi Wang⁵ 

¹Deep Space Exploration Laboratory, School of Earth and Space Sciences, University of Science and Technology of China, Hefei, China, ²CAS Key Laboratory of Geoscience Environment, School of Earth and Space Sciences, University of Science and Technology of China, Hefei, China, ³CAS Center for Excellence in Comparative Planetology, Hefei, China, ⁴Collaborative Innovation Center of Astronautical Science and Technology, Harbin, China, ⁵Physics Department, Auburn University, Auburn, AL, USA

Abstract Whistler mode chorus waves appear either as a series of discrete elements (rising or falling tones) or as banded hiss-like emissions in the dynamic spectrogram. Although the generation of rising-tone chorus waves has been extensively studied, few studies have focused on the generation of hiss-like emissions. In this paper, using the one-dimensional (1-D) general curvilinear particle-in-cell (gcPIC) simulation model, we have thoroughly studied the generation mechanisms of hiss-like emissions. Based on the spectrogram, we first classify hiss-like emissions into four types (I, II, III, and IV). We find that the type I hiss-like waves are linearly excited by the anisotropic electrons, while other types are excited through the nonlinear process. For the type I waves, they do not undergo a frequency chirping process and have a relatively broadband spectrum. The high proportion of hot electrons or the large temperature anisotropy of hot electrons will decrease the threshold for nonlinear growth and cause the wave amplitudes to exceed the threshold, leading to the nonlinear generation of type II hiss-like waves. The fresh hot electrons continually injected into the system with a large drift velocity significantly reduces the time interval between the rising tone elements to form a continuous spectrum, which are the type III waves. The intense and long-lasting hiss-like emissions, that is, type IV, which are the most frequently observed, should be generated due to the combined effect of the rapid injection and the high proportion of hot electrons (or the large temperature anisotropy). Our findings provide a comprehensive understanding of the generation of hiss-like chorus waves in the Earth's magnetosphere.

Plain Language Summary Chorus waves are important electromagnetic waves in the inner magnetosphere, which typically appears as either hiss-like emissions or discrete rising or falling tones. Although much effort has been spent on explaining the frequency chirping of chorus waves, the generation of hiss-like emissions have long been neglected, which are actually the more common spectrogram than the discrete ones. Based on Van Allen Probes data, we first reveal that the hiss-like emissions can be further divided into four types (I, II, III, and IV). Then, we utilize a one-dimensional general curvilinear particle-in-cell (gcPIC)- δf model to successfully reproduce the four types of hiss-like emissions. We propose that the type I hiss-like waves are linearly excited by the electrons with a temperature anisotropy, while other types undergo the nonlinear growth. The high proportion or large temperature anisotropy of hot electrons will cause the strong nonlinear growth, resulting in the generation of the type II hiss-like waves. The type III waves depend on the continuous injection of energetic electrons caused by the azimuthal drift. Due to the combined effect of the rapid injection and intense nonlinear growth, the intense and long-lasting hiss-like emissions, that is, type IV, which are the most frequently observed, are generated. Our findings provide a deeper insight of the generation of hiss-like chorus waves in the terrestrial magnetosphere.

1. Introduction

Whistler mode chorus waves are strong electromagnetic emissions frequently observed in the Earth's magnetosphere, typically falling within two distinct frequency bands: the upper band and the lower band, separated by a power gap around $0.5f_{ce}$ (where f_{ce} is the electron gyrofrequency at the equator) (Burtis & Helliwell, 1969; H. Chen, Gao, et al., 2022; Gao et al., 2017; Li et al., 2012; Tsurutani & Smith, 1974, 1977). Chorus waves are mainly generated near the geomagnetic equator (Lauben et al., 2002; LeDocq et al., 1998; Li et al., 2009), which is excited by the electrons with thermal anisotropy from the plasma sheet (Gao et al., 2014; Kennel & Petschek, 1966; Tsurutani & Smith, 1977). These waves play a critical role in precipitating ~ 0.1 –30 keV electrons into the atmos-

Table 1
The Initialization of 12 Runs

Run	$n_{h,eq}/n_0$	A_T	$\tau_D \Omega_{e0}$
1	0.0075	4.0	∞
2	0.01	4.0	∞
3	0.015	4.0	∞
4	0.02	4.0	∞
5	0.01	2.5	∞
6	0.01	3.8	∞
7	0.01	5.0	∞
8	0.01	7.0	∞
9	0.01	4.0	2,000
10	0.01	4.0	400
11	0.01	4.0	250
12	0.03	4.0	250

phere to produce the diffuse and pulsating aurora (Horne & Thorne, 2003; Miyoshi et al., 2010; Mozer et al., 2018; Ni et al., 2011; Thorne et al., 2010) and accelerating ~ 100 keV electrons to \sim MeV energies (Horne, 2005; Horne & Thorne, 2003; Reeves et al., 2013; Thorne et al., 2013).

Whistler mode chorus waves appear either as a series of discrete upward chirping (rising tones) and downward chirping (falling tones) or as hiss-like emissions in the dynamic spectrogram (Gao et al., 2014; Li et al., 2012). It is widely accepted that the generation of the discrete rising-tone chorus occurs due to the nonlinear resonant interactions between energetic electrons and whistler-mode waves, which has been supported by several numerical simulations (H. Chen, Lu, et al., 2022; Hikishima et al., 2009; Ke et al., 2017; Lu et al., 2019; Tao et al., 2017). However, few studies have focused on the generation of the hiss-like emissions, even though hiss-like emissions are pervasive in the Earth's magnetosphere. The statistical study using THEMIS data (Gao et al., 2014) demonstrated that the amplitude and occurrence of hiss-like emissions exhibit a positive correlation with the proportion of hot electrons, which is consistent with the expectation of the linear stability theory. With 1-D electron hybrid simulations, Katoh and Omura (2013) suggested that hiss-like emissions can be nonlinearly generated, especially

when the inhomogeneity of the geomagnetic field is very small. In addition, recent studies proposed that chorus waves with a continuous spectrum will be excited by the rapid injection of energetic electrons (Gao et al., 2022; Lu et al., 2021). So far, the generation mechanism of hiss-like emissions still remains unclear.

In this paper, with the one-dimensional (1-D) general curvilinear particle-in-cell (gcPIC) simulation model, we have thoroughly investigated the generation mechanism of hiss-like emissions. Based on Van Allen Probes data, we first classify hiss-like emissions into four types (I, II, III, IV) based on the dynamic spectrogram. We have successfully reproduced the four types of hiss-like emissions in our simulations, and uncovered the different generation mechanisms for each type. Our study provides new insight into the generation mechanism of hiss-like emissions in the Earth's magnetosphere.

2. Simulation Model and Data Set

We carry out numerical experiments with the 1-D gcPIC- δf simulation model in a dipole magnetic field. There are three kinds of particles in the model: background cold electrons, anisotropic hot electrons, and protons. The model regards all species as superparticles, but protons are motionless. The simulation domain is along a field line with the magnetic latitude ranging from -30° to 30° , and the topology of the background magnetic field is roughly equivalent to that at $L = 0.5$ for saving computation source. Unlike previous PIC models, hot electrons can be continuously injected into the system in the azimuthal direction. A detailed description of this model has been expounded in recent studies (H. Chen, Lu, et al., 2022; Lu et al., 2021).

The ratio between plasma frequency ω_{pe} ($=\sqrt{n_0 e^2/m_e \epsilon_0}$) and electron gyrofrequency Ω_{e0} ($=eB_0/m_e$) at the equatorial plane is set to 5.0, where n_0 is the plasma number density, and m_e is the electron mass, respectively. The cold electrons are isotropic with a temperature of 10 eV, while hot electrons satisfy a bi-Maxwellian distribution with the number density $n_{h,eq}$ at the equator. The number density $n_{h,eq}/n_0$ and temperature anisotropy A_T ($=T_{\perp,eq}/T_{\parallel,eq}$) at the equator ($T_{\perp,eq}$ and $T_{\parallel,eq}$ are the perpendicular and parallel temperatures of hot electrons at the equator) in different simulation runs are listed in Table 1.

The temperature anisotropy A_T is controlled by changing the perpendicular temperature $T_{\perp,eq}$ with the fixed $T_{\parallel,eq} = 0.5 m_e V_{th\parallel}^2$ ($V_{th\parallel} = 0.28c$ is the thermal velocity and c is the speed of light). The number density and temperature anisotropy of hot electrons along the field line satisfy the Liouville's theorem (Summers et al., 2012). The parameters used in our model are typical values at $L \sim 5$ in the Earth's magnetosphere. In our simulations, there are 4,000 grid cells along the field line. On average, there are about 4,000 particles per cell, and the time step is $0.02 \Omega_{e0}^{-1}$. The time scale of electron injection is determined by τ_D , which is also listed in Table 1 for different simulation runs. In runs 1–8, the time scale is set to $\tau_D \Omega_{e0} = \infty$, meaning that the electron injection is turned off, while in runs 9–12, smaller τ_D denotes the faster electron injection.

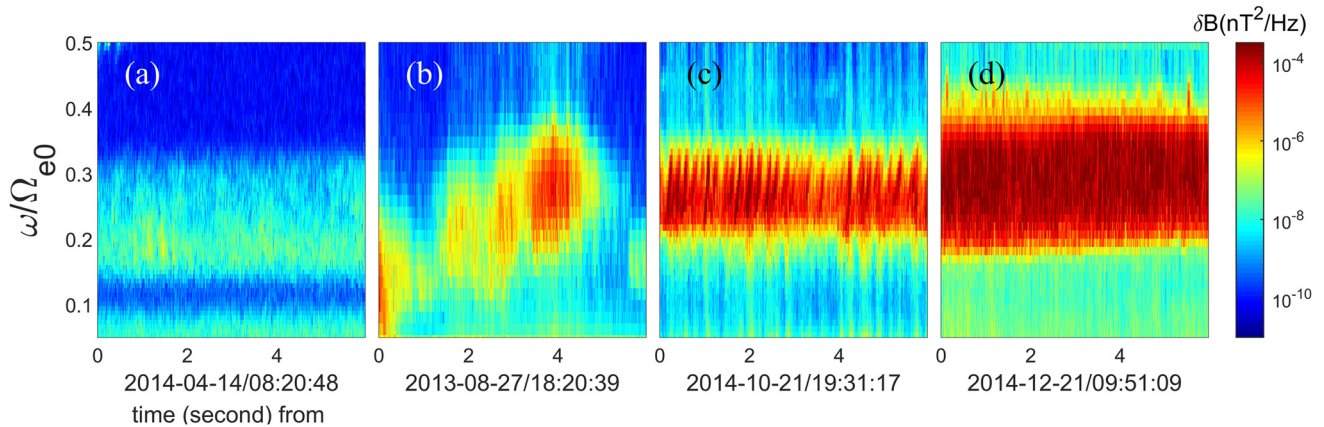


Figure 1. Four hiss-like emissions events observed by Van Allen Probe-A.

Van Allen Probes (Mauk et al., 2012), consisting of two identical satellites (A and B) in near-equatorial orbits with perigees of $\sim 1.1 R_E$ and apogees of $\sim 5.8 R_E$, completely cover the main source region (i.e., magnetic equator) of chorus waves. The high-resolution waveform data (35,000 samples/sec) is obtained from the onboard Electric and Magnetic Field Instrument Suite and Integrated Science (EMFISIS) instrument (Kletzing et al., 2013). The triaxial fluxgate magnetometer (MAG, a part of the EMFISIS instrument suite) measures the background magnetic field. The plasma data is collected from the Helium, Oxygen, Proton, and Electron instrument (Funsten et al., 2013).

3. Results

We select 1,780 hiss-like emissions events detected by Van Allen Probe-A from January 2013 to December 2014 and classify these waves into four types (I, II, III, IV) based on the dynamic spectrogram, as shown in Figure 1. It is worth noting that, as chorus waves propagate from the equator toward higher latitudes with enhanced wave normal angles and increasing parallel electric fields, the waves are severely damped through Landau resonance (L. Chen et al., 2013; Lu et al., 2019). Since the wave amplitude is an important selection criterion, we restricted the latitude to within $\pm 8^\circ$ and the wave normal angles to less than 30° to reduce the effect of Landau damping. Type I wave is the continuous broadband wave with weak amplitude (less than 40 pT) as shown in Figure 1a. Figure 1b shows type II wave: a hiss-like emission with a large amplitude (>40 pT) and a continuous spectrum, but a short duration (<4 s). Figure 1c depicts a continuous spectrum with a longer duration (>6 s) and larger amplitude (>40 pT), but with distinguishable individual rising-tone elements. Figure 1d shows the most typical hiss-like chorus event in observation (Gao et al., 2014; Li et al., 2012), with a wide frequency range, high amplitude (>60 pT), and long duration (>6 s). The hiss-like chorus waves shown in Figures 1c and 1d are classified as type III and IV respectively. For the type III wave, it is quite difficult to automatically recognize them due to the short time separation between rising tones, so we use the naked eye to check whether there are rising tones. In our database, the total number of wave events for four types (I, II, III, IV) is 482, 79, 301, and 918, respectively.

To investigate the generation mechanisms of different types of hiss-like emissions, we set up different simulation cases. Figures 2a–2d present the power spectral density (PSD) of magnetic fields at latitude $\lambda = 15^\circ$ in runs 1–4, where the electron injection is not considered. From run 1 to 4, the proportion of hot electrons is increasing but other parameters are fixed. In Figure 2a, there is no discrete element but a series of broadband whistler-mode emissions with relatively low magnetic power, consistent with the type I hiss-like emission. As $n_{h,eq}/n_0$ increases, a clear rising-tone element can be observed in Figure 2b. When the $n_{h,eq}/n_0$ is sufficiently large, the spectrum looks more like hiss-like emissions in Figures 2c and 2d than discrete rising-tone elements in Figure 2b. Moreover, the frequency range and wave amplitude in run 4 with higher $n_{h,eq}/n_0$ are larger than those in run 3, similar to the type II hiss-like emission. For runs 5–8, we increase the temperature anisotropy of hot electrons but fix their relative density, and find the transformation of the magnetic spectrum is the same as that in Figure 2 (not shown). The magnetic spectrum of runs 5 and 8 are consistent with those of type I and II hiss-like emissions, respectively.

Figure 3a displays the time-space profile of the wave magnetic field of northward-propagating waves in run 2, where S is the distance along the magnetic field line (normalized by the radius of gyration of electrons ρ_e). One

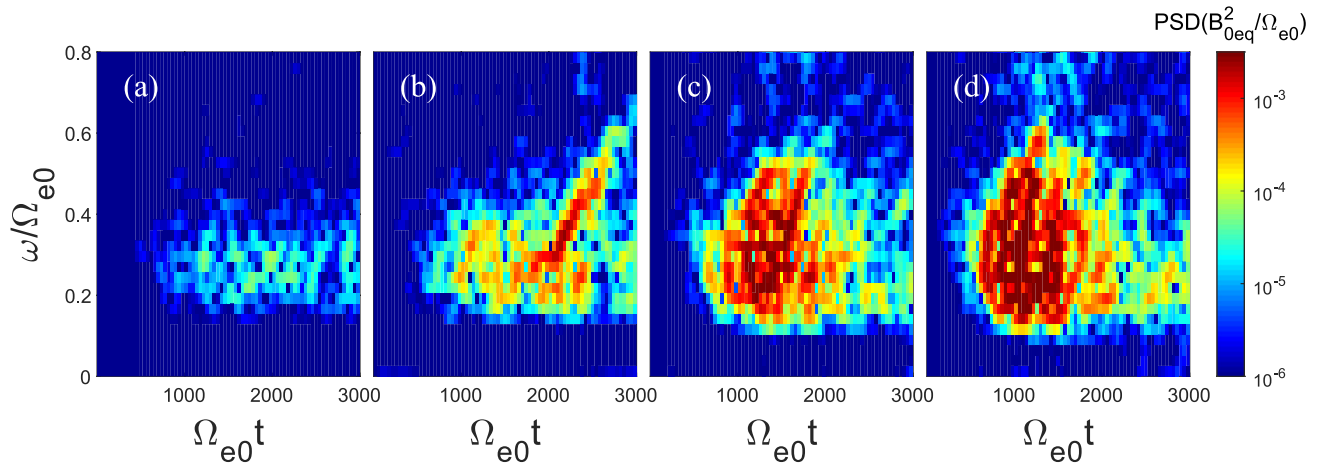


Figure 2. The spectrogram of the power spectral density of magnetic fields at the latitude $\lambda = 15^\circ$ in runs 1–4.

wave packet is extracted, marked by the blue shading (the width of the shading indicates the time window $\Delta t = 80 \Omega_{e0}^{-1}$) in Figure 3a. As illustrated in Figure 3b, the average wave amplitude gradually increases as the selected wave packet propagates away from the equator. Figure 3c shows the frequency of the wave packet, which is obtained by Fourier transforming the dominant wave amplitudes within the time window $\Delta t = 80 \Omega_{e0}^{-1}$ and amplitude-weighted averaging. The frequency of the wave packet remains almost constant, that is, $\sim 0.33\Omega_{e0}$. We obtained the temporal growth rate as $\Gamma_{Ns} = 1.14 \times 10^{-2}\Omega_{e0}$ near the equator, based on the amplitude variation along the magnetic field line and the group velocity V_g calculated by the cold plasma dispersion relation of the whistler mode wave within the magnetic latitude of 6° (the region between the two blue vertical lines in Figure 3b). The linear growth rate $\Gamma_L = 0.38 \times 10^{-2}\Omega_{e0}$ and nonlinear growth rate $\Gamma_N = 1.52 \times 10^{-2}\Omega_{e0}$ are also calculated based on Kennel and Petschek (1966) and Omura et al. (2008), respectively. It is worth noting that the depth of the electron hole is set as $Q = 0.5$ (Q is the depth of an electron hole due to depletion of trapped resonant electrons in the velocity phase space) in this study. This parameter can represent the intensity of wave particle resonance interaction. According to previous research results, the Q value is usually taken as 0.5, which means that half of the resonant electrons are captured (Omura, 2021). The growth rate is significantly larger than the linear growth rate and approaches the nonlinear growth rate. Although the growth rate is lower than that predicted by nonlinear theory, it is safe to say that the wave underwent a nonlinear growth process, as supported by the rising tone structure in Figure 2b.

Figure 4a shows the growth rate of the northward propagating wave packets in the equatorial region ($|\lambda| < 6^\circ$) for runs 1–4. The solid dots represent the wave growth rates in the simulations, which are calculated as mentioned above, and the asterisks and triangles represent the theoretically calculated linear and nonlinear growth rates, respectively. It is worth noting that we selected wave packets in each run with a frequency near $0.3\Omega_{ce}$ and the most intense amplitude in the s - t plane ($-15 < s/\rho_e < 215$, $800 < t \Omega_{e0} < 2,000$). Both the growth rate in the simulations and the theoretical growth rates gradually increase with the $n_{h,eq}n_0$. For run 1, the wave growth rate is comparable to the theoretical linear growth rate, while the wave growth rate is larger than the linear growth rate and approaches the nonlinear growth rate for runs 2–4. We suggest that runs 2–4 undergo a nonlinear growth process, while the wave is too weak to trigger such a nonlinear process in run 1. Figure 4b displays the peak wave amplitude of the frequency spectra at the equator ($\lambda = 0^\circ$) in runs 1–4. The peak wave amplitude is the peak value of the PSD for each frequency observed at the equator over the entire simulation time. The optimum amplitude and the threshold amplitude for the chorus waves in nonlinear theory (Omura & Nunn, 2011; Omura et al., 2009) are also plotted in Figure 4b, which are identified by dashed lines and dotted lines, respectively. The equation of the threshold amplitude $B_{w,th}$ is given by

$$\frac{B_{w,th}}{B_0} = \tilde{\Omega}_{th}, \quad (1)$$

and

$$\tilde{\Omega}_{th} = \frac{100\pi^3\xi}{\tilde{\omega}_{ph}^4\tilde{V}_{\perp 0}^5\mathcal{X}^5} \left(\frac{\tilde{a}s_2\tilde{U}_{\parallel}}{Q} \right)^2 \exp\left(\frac{\tilde{V}_R^2}{\tilde{U}_{\parallel}^2} \right) \quad (2)$$

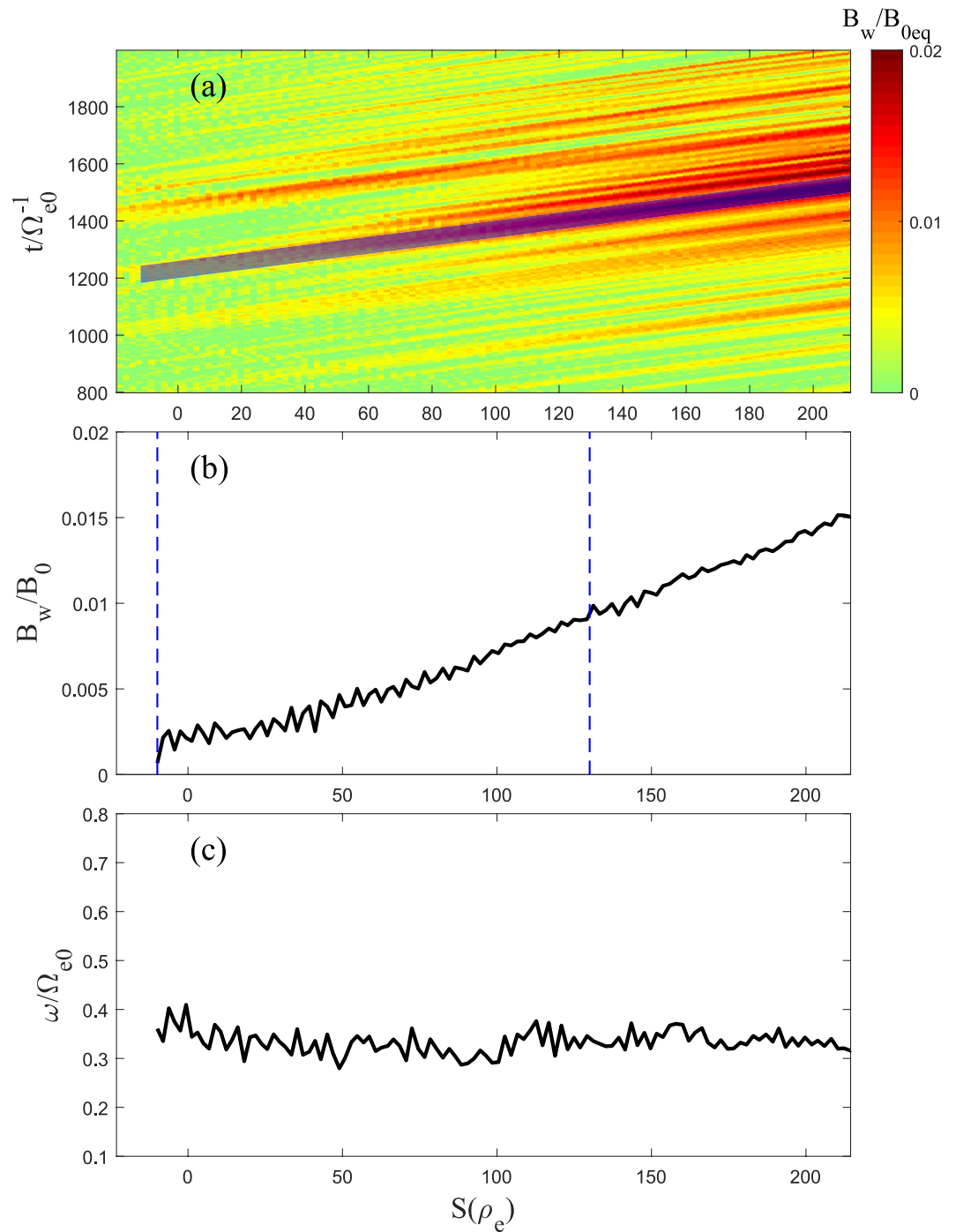


Figure 3. (a) The time-space profile of the wave magnetic field of northward-propagating waves in run 2. Spatial profiles of (b) wave amplitude and (c) averaged frequency of the wave packet indicated by the blue shading.

Where B_0 is the background magnetic field, $\xi^2 = \omega(\Omega_e - \omega)/\omega_{pe}^2$, $\tilde{\omega} = \omega/\Omega_{e0}$, $\tilde{\omega}_{ph} = \omega_{ph}/\Omega_{e0}$, $\omega_{ph} = \omega_{pe}(N_{e,hot}/N_{e,cold})^{1/2}$, $\tilde{V}_{L0} = V_{L0}/c$, $\chi = (1 + \xi^2)^{-1/2}$,

$$s_2 = \frac{1}{2\xi\chi} \left[\frac{\omega}{\Omega_e} \left(\frac{V_{L0}}{c} \right)^2 - (2 + \chi^2) \frac{V_R V_p}{c^2} \right] \quad (3)$$

V_R is the resonance velocity, V_p is the phase velocity, $\tilde{U}_{\parallel} = V_{h\parallel}/c$, $\tilde{V}_R = V_R/c$. $\tilde{a} = ac^2/\Omega_{e0}^2$ is related to the magnetic field inhomogeneity along a field line. For a dipole magnetic field, the parameter is $a = 4.5/(LR_p)^2$

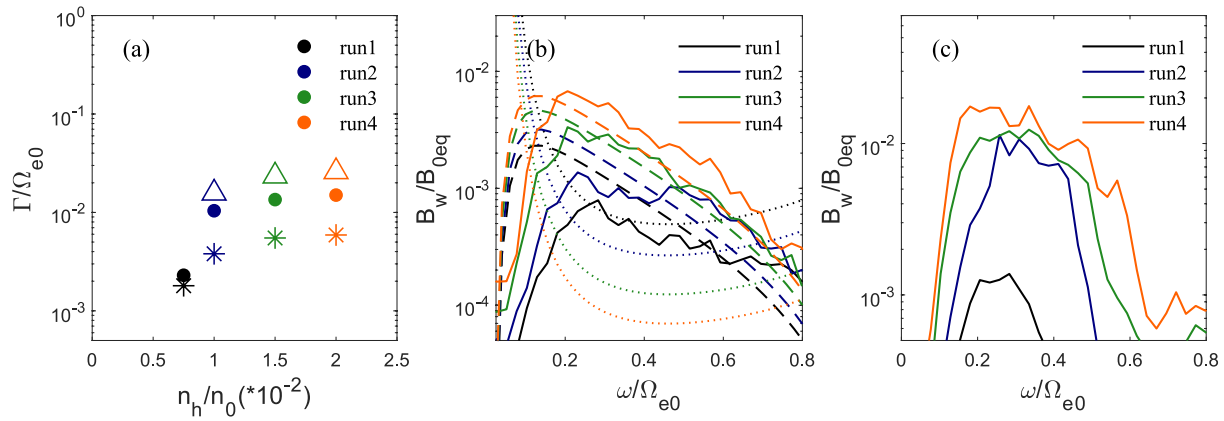


Figure 4. (a) The growth rate of the northward-propagating wave packets in the equatorial region ($|\lambda| < 6^\circ$) for runs 1–4. The solid dots represent the wave growth rates in the simulations, and the asterisks and triangles represent the theoretically calculated linear and nonlinear growth rates, respectively. (b) The peak, optimum and threshold amplitudes of the frequency spectra at the equator ($\lambda = 0^\circ$) in runs 1–4. The dotted and dashed lines represent the threshold amplitude and optimum amplitude with parameters $Q = 0.5$ and $\tau = 1.0$, respectively. (c) The peak wave amplitude of the frequency spectra at latitude $\lambda = 15^\circ$ in runs 1–4.

where L is the L-shell and R_p is the planet radius (Ke et al., 2020). In our simulation, the value \tilde{a} is set as $\tilde{a} = 6.24 \times 10^{-5}$. The optimum wave amplitude $B_{w,opt}$ normalized by Ω_{e0} , $B_{w,opt} = \Omega_{opt}/\Omega_{e0}$, is given by

$$\tilde{\Omega}_{opt} = 0.81\pi^{-5/2} \frac{Q}{\tau} \frac{s_1 \tilde{V}_g}{s_0 \tilde{\omega} \tilde{U}_{\parallel}} (\tilde{\omega}_{ph} \tilde{V}_{L0} \chi)^2 \exp\left(-\frac{\tilde{V}_R^2}{2\tilde{U}_{\parallel}^2}\right), \quad (4)$$

Where τ is the ratio of the nonlinear transition time T_N , the time scale of formation of an electromagnetic electron hole in the velocity phase space, to the nonlinear trapping period $T_{tr} = 2\pi/\omega_{tr}$, where ω_{tr} is the trapping frequency (Omura & Nunn, 2011), and $\tilde{V}_g = V_g/c$. The parameter τ is set as $\tau = 1.0$. For run 1, the peak amplitude is lower than the threshold amplitude, which also means it is difficult for the wave to trigger the nonlinear process. While, the peak amplitude exceeds the threshold amplitude and is close to the optimum amplitude for runs 2–4, which is another evidence that the waves in runs 2–4 enter nonlinear growth progress. Figure 4c displays the peak wave amplitude of the frequency spectra at latitude $\lambda = 10^\circ$ in runs 1–4. The increase in wave frequency width is more significant than the enhancement of the wave amplitude with the $n_{h,eq}/n_0$. This is due to the growth of the waves saturates at a certain frequency, but grows nonlinearly over a larger frequency range. Based on the same analysis, we find that the waves in run 5 do not enter the nonlinear phase, while those in runs 6–8 undergo nonlinear growth. Therefore, we suggest that the type I hiss-like emission is linearly excited and the type II hiss-like emission is nonlinearly excited without the electron injection.

The influence of the electron injection on the generation mechanism of hiss-like emissions is studied by performing runs 9–12. Figures 5a–5c present the PSD of magnetic fields at latitude $\lambda = 10^\circ$ in runs 9–11. There are a

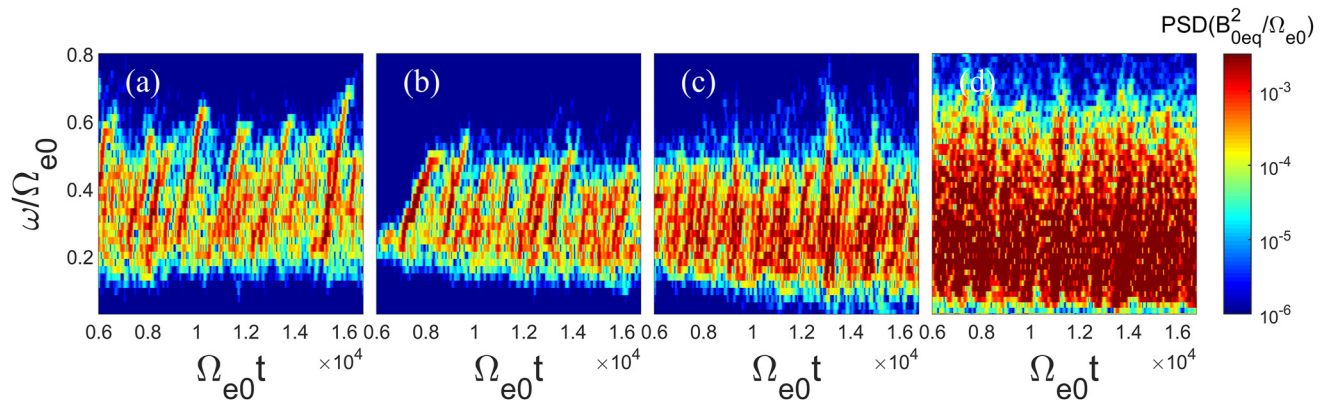


Figure 5. The spectrogram of the power spectral density of magnetic fields at latitude $\lambda = 10^\circ$ in runs 9–12.

series of chorus waves with a rising chirping shown in Figures 5a and 5b, which is similar to Lu et al. (2021). As $\tau_D \Omega_{e0}$ decreases, the spectrogram gradually shifts from the repetitive rising tone elements to an almost continuous spectrum (i.e., hiss-like chorus), similar to the type III hiss-like emission, as shown in Figure 5c. We combine the strong injection of electrons with a large hot electron density to set up run 12. The spectrum of run 12 exhibits a continuous spectrum with a wider frequency and larger amplitude than other runs as shown in Figure 5d, which is consistent with the type IV hiss-like emission. Based on Lu et al. (2021), the electron hole also exists in the electron distributions for the rising-tone chorus with a continuous spectrum, therefore, the type III and IV hiss-like emissions evolving from the continuous rising-tone chorus also undergo nonlinear growth.

4. Summary and Discussion

In this study, the generation mechanism of hiss-like emissions has been thoroughly investigated by using the one-dimensional (1-D) general curvilinear particle-in-cell (gcPIC) simulation code. Based on Van Allen Probes data, we first classify hiss-like emissions into four types (I, II, III, IV) based on the dynamic spectrogram. We have successfully reproduced the four types of hiss-like emissions in our simulations, and uncovered the different generation mechanisms for each type. The type I hiss-like emission is linearly excited and the type II hiss-like emission is nonlinearly excited without the electron injection. For the type II hiss-like emissions, the high proportion of hot electrons or the large temperature anisotropy of hot electrons will decrease the threshold for nonlinear growth and cause the wave amplitudes significantly exceed the threshold, leading to the nonlinear generation waves. Moreover, with the increase of the number density or the temperature anisotropy of hot electrons, the increase in wave frequency width is more significant than the enhancement of the wave amplitude. For the type III waves, the fresh hot electrons continually injected into the system with a large drift velocity significantly reduces the time interval between the rising tone elements to form a continuous spectrum. For the types IV hiss-like emissions, they are nonlinearly excited with the strong injection of electrons and the latter also requires a large hot electron density or a large temperature anisotropy. It is worth noting that due to the higher numerical noise and limited computing source, it is common to use the larger temperature anisotropy in the simulations to speed up the process (Devine et al., 1995; Lu et al., 2019; Omura et al., 2008), which also leads to the larger growth rates of whistler-mode waves. Therefore, the amplitude and bandwidth of waves in the simulations are usually larger than the observed waves. In our database, the total number of wave events for four types (I, II, III, IV) is 482, 79, 301, and 918, respectively. To summarize, the majority of hiss-like chorus waves in the Earth's magnetosphere are generated through a nonlinear process and most of them are accompanied by the rapid injection of hot electrons with the high flux.

Gao et al. (2014) found that the wave amplitudes of hiss-like chorus waves are closely correlated with the ratio of hot electron density to total electron density (N_h/N_t). In this study, we found that when $n_{h,eq}/n_0$ (corresponding to N_h/N_t in the observation) is small, the waves grow in the linear stage, while, as $n_{h,eq}/n_0$ increases, the waves enter the nonlinear generation process. Whether the waves undergo the linear or nonlinear growth process, their growth rate is directly proportional to $n_{h,eq}/n_0$, which provides an explanation for the observation results by Gao et al. (2014). Other studies indicated that the hiss-like chorus can be also caused by the continuous injection of energetic electrons (Gao et al., 2022; Lu et al., 2021), which is verified in our paper. Moreover, the statistical analysis demonstrates that the majority of hiss-like events occur in the region from the midnight to the dawn sector (Gao et al., 2014), where the proportion of energetic electrons and drift velocities are relatively high (Gao et al., 2022), which supports our study. Katoh and Omura (2013) suggested that the hiss-like emissions are nonlinearly generated, when the geomagnetic field inhomogeneity is very small. Similarly, with a smaller magnetic field gradient, "broadband" EMIC bursts are observed in the simulation, which is like the hiss-like spectrum (Shoji & Omura, 2014). However, satellite observations show that the occurrence rate of hiss-like emissions peaks in the midnight-dawn sector rather than the noon sector where the geomagnetic field inhomogeneity is minimum. Hence, we speculate that the most crucial factors influencing the excitation of hiss-like emissions are the rapid injection of electrons and the number density of hot electrons. In this paper, we have summarized four mechanisms for the excitation of hiss-like waves, which is helpful in understanding the generation of chorus waves.

Data Availability Statement

The entire Van Allen Probes data set is publicly available at <https://spdf.gsfc.nasa.gov/pub/data/rbsp/>. The Van Allen Probe data analysis is carried out using the publicly available Space Physics Environment Data Analysis Software (SPEDAS, <http://spedas.org>). The simulation data (Kong, 2023) are available at <https://doi.org/10.57760/sciencedb.08125>.

Acknowledgments

This work was supported by the NSFC Grant 42230201, Fundamental Research Funds for the Central Universities (WK3420000013), B-type Strategic Priority Program of the Chinese Academy of Sciences, Grant XDB41000000, and "USTC Tang Scholar" program. We acknowledge the entire Van Allen Probes instrument teams. We also acknowledge the data resources from National Space Science Data Center, National Science & Technology Infrastructure of China (<http://www.nssdc.ac.cn>).

References

- Burtis, W. J., & Helliwell, R. A. (1969). Banded chorus—A new type of VLF radiation observed in the magnetosphere by OGO 1 and OGO 3. *Journal of Geophysical Research*, 74(11), 3002–3010. <https://doi.org/10.1029/JA074i011p03002>
- Chen, H., Gao, X., Lu, Q., Fan, K., Ke, Y., Wang, X., & Wang, S. (2022). Gap formation around 0.5 Ω_e in the whistlermode waves due to the plateau-like shape in the parallel electron distribution: 2D PIC simulations. *Journal of Geophysical Research: Space Physics*, 127(5), e2021JA030119. <https://doi.org/10.1029/2021ja030119>
- Chen, H., Lu, Q., Wang, X., Fan, K., Chen, R., & Gao, X. (2022). One-dimensional gcPIC- δf simulation of hooked chorus waves in the Earth's inner magnetosphere. *Geophysical Research Letters*, 49(4), e2022GL097989. <https://doi.org/10.1029/2022gl097989>
- Chen, L., Thorne, R. M., Li, W., & Bortnik, J. (2013). Modeling the wave normal distribution of chorus waves. *Journal of Geophysical Research: Space Physics*, 118(3), 1074–1088. <https://doi.org/10.1029/2012ja018343>
- Devine, P. E., Chapman, S. C., & Eastwood, J. W. (1995). One- and two-dimensional simulations of whistler mode waves in an anisotropic plasma. *Journal of Geophysical Research*, 100(A9), 17189–17203. <https://doi.org/10.1029/95ja00842>
- Funsten, H. O., Skoug, R. M., Guthrie, A. A., MacDonald, E. A., Baldonado, J. R., Harper, R. W., et al. (2013). Helium, Oxygen, Proton, and Electron (HOPE) Mass Spectrometer for the radiation belt storm probes mission. *Space Science Reviews*, 179(1–4), 423–484. <https://doi.org/10.1007/s11214-013-9968-7>
- Gao, X., Chen, R., Lu, Q., Chen, L., Chen, H., & Wang, X. (2022). Observational evidence for the origin of repetitive chorus emissions. *Geophysical Research Letters*, 49(12), e2022GL099000. <https://doi.org/10.1029/2022gl099000>
- Gao, X., Ke, Y., Lu, Q., Chen, L., & Wang, S. (2017). Generation of multiband chorus in the Earth's magnetosphere: 1-D PIC simulation. *Geophysical Research Letters*, 44(2), 618–624. <https://doi.org/10.1002/2016gl072251>
- Gao, X., Li, W., Thorne, R. M., Bortnik, J., Angelopoulos, V., Lu, Q., et al. (2014). New evidence for generation mechanisms of discrete and hiss-like whistler mode waves. *Geophysical Research Letters*, 41(14), 4805–4811. <https://doi.org/10.1002/2014gl060707>
- Hikishima, M., Yagitani, S., Omura, Y., & Nagano, I. (2009). Full particle simulation of whistler-mode rising chorus emissions in the magnetosphere. *Journal of Geophysical Research*, 114(A1), A01203. <https://doi.org/10.1029/2008ja013625>
- Horne, R. B. (2005). Timescale for radiation belt electron acceleration by whistler mode chorus waves. *Journal of Geophysical Research*, 110(A3), A03225. <https://doi.org/10.1029/2004ja010811>
- Horne, R. B., & Thorne, R. M. (2003). Relativistic electron acceleration and precipitation during resonant interactions with whistler-mode chorus. *Geophysical Research Letters*, 30(10), 1527. <https://doi.org/10.1029/2003gl016973>
- Katoh, Y., & Omura, Y. (2013). Effect of the background magnetic field inhomogeneity on generation processes of whistler-mode chorus and broadband hiss-like emissions. *Journal of Geophysical Research: Space Physics*, 118(7), 4189–4198. <https://doi.org/10.1002/jgra.50395>
- Ke, Y., Gao, X., Lu, Q., Wang, X., & Wang, S. (2017). Generation of rising-tone chorus in a two-dimensional mirror field by using the general curvilinear PIC code. *Journal of Geophysical Research: Space Physics*, 122(8), 8154–8165. <https://doi.org/10.1002/2017ja024178>
- Ke, Y., Lu, Q., Gao, X., Wang, X., Chen, L., Wang, S., et al. (2020). Particle-in-cell simulations of characteristics of rising-tone chorus waves in the inner magnetosphere. *Journal of Geophysical Research: Space Physics*, 125(7), e2020JA027961. <https://doi.org/10.1029/2020ja027961>
- Kennel, C. F., & Petschek, H. E. (1966). Limit on stably trapped particle fluxes. *Journal of Geophysical Research*, 71(1), 1–28. <https://doi.org/10.1029/JZ071i001p00001>
- Kletzing, C. A., Kurth, W. S., Acuna, M., MacDowall, R. J., Torbert, R. B., Averkamp, T., et al. (2013). The Electric and Magnetic Field Instrument Suite and Integrated Science (EMFISIS) on RBSP. *Space Science Reviews*, 179(1–4), 127–181. <https://doi.org/10.1007/s11214-013-9993-6>
- Kong, Z. (2023). Data for the Hiss-like Chorus (Version V1) [Dataset]. Science Data Bank. <https://doi.org/10.57760/sciencedb.08125>
- Lauben, D. S., Inan, U. S., Bell, T. F., & Gurnett, D. A. (2002). Source characteristics of ELF/VLF chorus. *Journal of Geophysical Research*, 107(A12), SMP 10-1–SMP 10-17. <https://doi.org/10.1029/2000ja003019>
- LeDocq, M. J., Gurnett, D. A., & Hospodarsky, G. B. (1998). Chorus source locations from VLF Poynting flux measurements with the Polar spacecraft. *Geophysical Research Letters*, 25(21), 4063–4066. <https://doi.org/10.1029/1998gl900071>
- Li, W., Thorne, R. M., Angelopoulos, V., Bortnik, J., Cully, C. M., Ni, B., et al. (2009). Global distribution of whistler-mode chorus waves observed on the THEMIS spacecraft. *Geophysical Research Letters*, 36(9), L09104. <https://doi.org/10.1029/2009gl037595>
- Li, W., Thorne, R. M., Bortnik, J., Tao, X., & Angelopoulos, V. (2012). Characteristics of hiss-like and discrete whistler-mode emissions. *Geophysical Research Letters*, 39(18), L18106. <https://doi.org/10.1029/2012gl053206>
- Lu, Q., Chen, L., Wang, X., Gao, X., Lin, Y., & Wang, S. (2021). Repetitive emissions of rising-tone chorus waves in the inner magnetosphere. *Geophysical Research Letters*, 48(15), e2021GL094979. <https://doi.org/10.1029/2021gl094979>
- Lu, Q., Ke, Y., Wang, X., Liu, K., Gao, X., Chen, L., & Wang, S. (2019). Two-dimensional gcPIC simulation of rising-tone chorus waves in a dipole magnetic field. *Journal of Geophysical Research: Space Physics*, 124(6), 4157–4167. <https://doi.org/10.1029/2019ja026586>
- Mauk, B. H., Fox, N. J., Kanekal, S. G., Kessel, R. L., Sibeck, D. G., & Ukhorskiy, A. (2012). Science objectives and rationale for the radiation belt storm probes mission. *Space Science Reviews*, 179(1–4), 3–27. <https://doi.org/10.1007/s11214-012-9908-y>
- Miyoshi, Y., Katoh, Y., Nishiyama, T., Sakanoi, T., Asamura, K., & Hiraehara, M. (2010). Time of flight analysis of pulsating aurora electrons, considering wave-particle interactions with propagating whistler mode waves. *Journal of Geophysical Research*, 115(A10), A10312. <https://doi.org/10.1029/2009ja015127>
- Mozer, F. S., Agapitov, O. V., Blake, J. B., & Vasko, I. Y. (2018). Simultaneous observations of lower band chorus emissions at the equator and microburst precipitating electrons in the ionosphere. *Geophysical Research Letters*, 45(2), 511–516. <https://doi.org/10.1002/2017gl076120>
- Ni, B., Thorne, R. M., Shprits, Y. Y., Orlova, K. G., & Meredith, N. P. (2011). Chorus-driven resonant scattering of diffuse auroral electrons in nondipolar magnetic fields. *Journal of Geophysical Research*, 116(A6), A06225. <https://doi.org/10.1029/2011ja016453>
- Omura, Y. (2021). Nonlinear wave growth theory of whistler-mode chorus and hiss emissions in the magnetosphere. *Earth, Planets and Space*, 73(1), 95. <https://doi.org/10.1186/s40623-021-01380-w>
- Omura, Y., Hikishima, M., Katoh, Y., Summers, D., & Yagitani, S. (2009). Nonlinear mechanisms of lower-band and upper-band VLF chorus emissions in the magnetosphere. *Journal of Geophysical Research*, 114(A7), A07217. <https://doi.org/10.1029/2009ja014206>
- Omura, Y., Katoh, Y., & Summers, D. (2008). Theory and simulation of the generation of whistler-mode chorus. *Journal of Geophysical Research*, 113(A4), A04223. <https://doi.org/10.1029/2007JA012622>
- Omura, Y., & Nunn, D. (2011). Triggering process of whistler mode chorus emissions in the magnetosphere. *Journal of Geophysical Research*, 116(A5), A05205. <https://doi.org/10.1029/2010ja016280>
- Reeves, G. D., Spence, H. E., Henderson, M. G., Morley, S. K., Friedel, R. H. W., Funsten, H. O., et al. (2013). Electron acceleration in the heart of the Van Allen radiation belts. *Science*, 341(6149), 991–994. <https://doi.org/10.1126/science.1237743>
- Shoji, M., & Omura, Y. (2014). Spectrum characteristics of electromagnetic ion cyclotron triggered emissions and associated energetic proton dynamics. *Journal of Geophysical Research: Space Physics*, 119(5), 3480–3489. <https://doi.org/10.1002/2013ja019695>

- Summers, D., Omura, Y., Miyashita, Y., & Lee, D.-H. (2012). Nonlinear spatiotemporal evolution of whistler mode chorus waves in Earth's inner magnetosphere. *Journal of Geophysical Research*, *117*(A9), A09206. <https://doi.org/10.1029/2012ja017842>
- Tao, X., Zonca, F., & Chen, L. (2017). Identify the nonlinear wave-particle interaction regime in rising tone chorus generation. *Geophysical Research Letters*, *44*(8), 3441–3446. <https://doi.org/10.1002/2017gl072624>
- Thorne, R. M., Li, W., Ni, B., Ma, Q., Bortnik, J., Chen, L., et al. (2013). Rapid local acceleration of relativistic radiation-belt electrons by magnetospheric chorus. *Nature*, *504*(7480), 411–414. <https://doi.org/10.1038/nature12889>
- Thorne, R. M., Ni, B., Tao, X., Horne, R. B., & Meredith, N. P. (2010). Scattering by chorus waves as the dominant cause of diffuse auroral precipitation. *Nature*, *467*(7318), 943–946. <https://doi.org/10.1038/nature09467>
- Tsurutani, B. T., & Smith, E. J. (1974). Postmidnight chorus: A substorm phenomenon. *Journal of Geophysical Research*, *79*(1), 118–127. <https://doi.org/10.1029/JA079i001p00118>
- Tsurutani, B. T., & Smith, E. J. (1977). Two types of magnetospheric ELF chorus and their substorm dependences. *Journal of Geophysical Research*, *82*(32), 5112–5128. <https://doi.org/10.1029/JA082i032p05112>